Computer Methods and Programs in Biomedicine 282 (2026) 109385

Contents lists available at ScienceDirect

Computer Methods and Programs in Biomedicine

journal homepage: https://www.sciencedirect.com/journal/computer-methods-and-programs-in-biomedicine

MRI-based CFD simulations of transient blood flow in compliant aortas using the LDDMM framework

Daiqi Lin [a,b], Jos Westenberg [c], Hildo Lamb [c], Saša Kenjereš [a,b,*]

[a] Department of Chemical Engineering, Faculty of Applied Sciences, Delft University of Technology, Delft, The Netherlands
[b] J.M. Burgerscentrum Research School for Fluid Mechanics, Delft, The Netherlands
[c] Department of Radiology, Leiden University Medical Center, Leiden, The Netherlands

ARTICLE INFO

Keywords:
Moving aortic wall simulation
Thoracic aortic aneurysm
LDDMM
Shape registration
Computational fluid dynamics (CFD)

ABSTRACT

Background: Traditional CFD analyses often rely on static (rigid) vascular geometries, which neglect the physiologically relevant motion of the aortic wall. This simplification can lead to inaccuracies in estimating key hemodynamic biomarkers, such as wall shear stress (WSS) and oscillatory shear index (OSI).
Methods: This study introduces the Large Deformation Diffeomorphic Metric Mapping (LDDMM) method to enable computationally efficient simulations of transient blood flow in compliant, subject- and patient-specific aortas derived from 4D Flow MRI data. The proposed framework simplifies CFD pre-processing, improves morphing accuracy, and enables physiologically realistic motion of the thoracic aorta, including its side-branches. The method was applied to two aortic geometries: a healthy case (HC) and a case with thoracic aortic aneurysm (TAA) located in the ascending region.
Results: The results were compared with those obtained from fixed aortic geometries extracted at peak systole. Hemodynamic biomarkers showed significant differences between static and moving geometries. For the healthy case (HC), the differences were 18% for the time-averaged wall shear stress (TAWSS) and 46% for the oscillatory shear index (OSI). For the thoracic aorta aneurysm (TAA) case, the corresponding values were 14% and 47%, respectively.
Conclusion: These findings highlight the importance of incorporating aortic wall motion in hemodynamic simulations. The developed LDDMM-based framework can be readily extended to other imaging modalities, such as ultrasound or computed tomography, and is recommended for future CFD analyses of compliant aortas.

1. Introduction

A thoracic aortic aneurysm (TAA) is a localized dilation of the arterial wall [1–4]. In clinical practice, treatment decisions are typically guided by the aneurysm's diameter and growth rate when assessing the need for surgery. However, relying solely on these simple criteria reduces patient specificity and limits the accuracy of treatment planning. Over the past decades, the integration of medical imaging with computational fluid dynamics (CFD) has emerged as a powerful approach to obtain blood flow velocity fields with high spatiotemporal resolution and to identify novel biomarkers for surgical planning, [5,6]. Despite this progress, most studies continue to relay on the rigid-wall assumption to simplify patient-specific simulations.

Generally, two main approaches are used to account for vascular wall motion in CFD simulations: fluid–structure interaction (FSI) simulation and image-based compliant CFD. Compared to conventional fluid–structure interaction (FSI) simulations [7–11], the image-based compliant CFD approach [12–15] overcomes several limitations of FSI, including the lack of detailed information on aortic wall properties (e.g. heterogeneous thickness and elasticity), difficulties in prescribing physiological boundary conditions, and the high computational cost and time requirements.

The image-based compliant CFD simulations framework for studying blood flow in TAAs, known as the moving-boundary method (MBM), was introduced by Capellini et al. [16]. The MBM incorporates vascular wall motion into CFD simulations through radial basis functions (RBF) mesh morphing. Since then, several studies in the literature have applied this method to investigate flow in the ascending aorta. For example, the MBM was applied to incorporate patient-specific changes in aortic geometry during the cardiac cycle and to perform transient CFD simulations [17]. More recently, this method was also used to study large-scale flow coherence in the ascending aorta [18]. In both studies, however, only the movement of the ascending aorta was

* Corresponding author at: Department of Chemical Engineering, Faculty of Applied Sciences, Delft University of Technology, Delft, The Netherlands.
E-mail addresses: d.l.lin@tudelft.nl (D. Lin), s.kenjeres@tudelft.nl (S. Kenjereš).

https://doi.org/10.1016/j.cmpb.2026.109385
Received 12 December 2025; Received in revised form 16 April 2026; Accepted 16 April 2026
Available online 27 April 2026

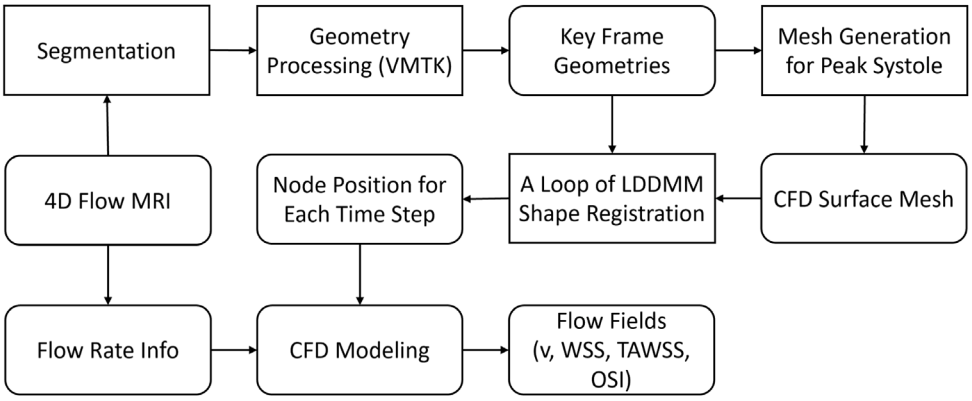

Fig. 1. Workflow for image-based moving-wall simulation using the Large Deformation Diffeomorphic Metric Mapping (LDDMM) method.

considered, while the remaining regions of the aorta were modeled as rigid.

Our previous study was the first to attempt incorporating the motion of the thoracic aorta into CFD simulations, [12]. Although mesh morphing was applied to the ascending aorta, descending aorta, and aortic arch, the branches were still modeled as rigid because defining control point locations in these relatively small vessels was constrained by the resolution of MRI data. Another limitation was that control points were distributed circumferentially at equal intervals within each cross-section along the centerline. Furthermore, the placement of these points required some additional manual adjustments, making the method more user-dependent in practical applications.

In essence, the core of previous works [12,16–18] lies in shape registration, an extended application of image registration. Shape/image registration is the process of determining a spatial transformation that aligns the feature points of two shapes or images so that their spatial positions and anatomical structures correspond consistently [19]. Typical deformation models include: (1) elastic models, (2) viscous fluid flow models, (3) optical flow models, and (4) models based on prior knowledge. However, in our previous study [12], this perspective was not explicitly acknowledged, and consequently the methods and resources from the field of shape/image registration were not fully exploited.

Hence, building on these insights, the present study proposes a novel image-based compliant CFD simulation method that incorporates the motion of the thoracic aorta to investigate blood flow fields in both a TAA case and a healthy case (HC). To achieve this, we employ the framework of large deformation diffeomorphic metric mapping (LDDMM), a technique from the field of medical image registration, to morph the CFD surface mesh. In recent studies [20,21], the LDDMM framework has primarily been utilized to construct statistical shape models for CFD-informed machine learning applications. To the best of our knowledge, the present study represents the first application of the LDDMM framework to generate time-resolved mesh deformations for high-fidelity, image-based moving-boundary CFD simulations of the aorta.

2. Method

The entire workflow of the developed method is shown in Fig. 1. Starting with approximately 6000 control points distributed in the ambient space surrounding the aorta, the locations and corresponding momenta vectors are optimized using the LDDMM framework to accurately represent the MRI-based movement of the thoracic aorta. Key methodological details are presented in the follow-up subsections.

2.1. Geometry processing

The aortic geometries analyzed in this work are derived from our previous study, which included both a thoracic aortic aneurysm (TAA) in the aortic root and a healthy aorta case (HC), [12]. For both cases, 4D-Flow MRI acquisitions were performed on a 3T MRI scanner (Elition, Philips Healthcare, Best, The Netherlands) using a hemidiaphragmatic respiratory navigator and retrospective electrocardiogram gating, without employing echo-planar imaging (EPI) technique. The acquired 4D-Flow MRI datasets were segmented using CAAS MR Solutions v5.2 (Pie Medical Imaging BV, Maastricht, The Netherlands). Note that the same segmentation protocol was applied for both subjects. Detailed characteristics of the patient, the healthy volunteer, and the 4D-Flow MRI sequence are provided in our previous work, [12]. Due to the limited spatial resolution of MRI and the low phase contrast during diastole, it is challenging to capture geometries in that period. Therefore, four frames were extracted for the HC case and eight frames for the TAA case from the MRI data. During diastole, the aortic geometries are assumed to remain the same as in early diastole, as previously adopted in [12]. Following acquisition, the raw geometries were pre-processed using the open-source software Vascular Modeling Toolkit (VMTK) [22] for simulation purposes. Pre-processing steps included remeshing, smoothing, subdivision, flow-extension, and capping. The resulting geometries after VMTK processing are denoted as $S_{\mathrm{MRI},i}$, where i indicates the MRI phase number.

The geometries of the HC and TAA cases at peak systole, after processing, are shown in Fig. 2. For the HC case, the inlet diameter is 29 mm and the total centerline length is 352 mm. For the TAA case, the inlet diameter is 31 mm, the diameter of the aortic root aneurysm is 50 mm, and the total centerline length is 324 mm. Notably, in this study no flow extensions were added to the TAA, whereas 15 mm flow extensions were added to the branches of the HC to elongate them.

Following VMTK processing, the geometry at peak systole was used to generate meshes for the CFD simulations using the software ICEM-CFD (Ansys, Canonsburg, PA, USA). Based on the mesh dependency study in [12], tetrahedral elements with a size of 1.8 mm and refinement near the wall were generated within the aortic lumen. The surface mesh of the CFD model was then extracted using an in-house code (denoted as S_{CFD}), and subsequently deformed to match the MRI geometries at different time instants, as described in the following subsection.

2.2. Surface mesh deformation

The predefinition of wall movement is central to this study and is achieved through surface mesh deformation. We employed a shape registration method based on LDDMM to deform the surface mesh and prescribe the wall movement at each time step (Δt = 0.001 s). The

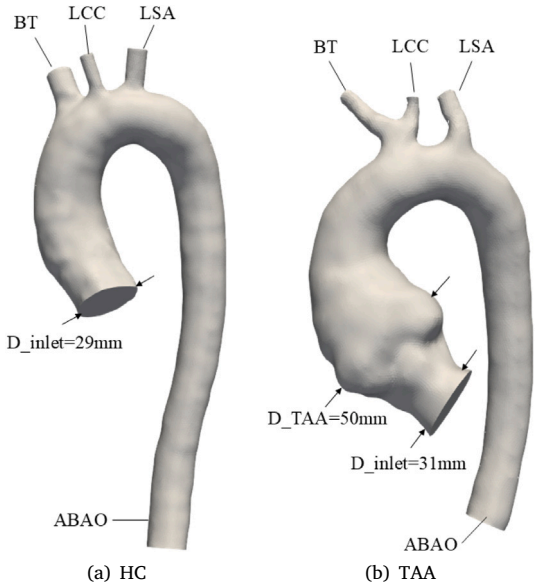

(a) HC (b) TAA

Fig. 2. Geometry at peak systole after the final pre-processing step for the healthy case (HC) and thoracic aortic aneurysm (TAA) cases. BT- brachiocephalic trunk, LCC- left common carotid artery, LSA- left subclavian artery, ABAO- abdominal aorta.

objective of LDDMM-based shape registration is to deform the CFD surface mesh S_{CFD} into the corresponding MRI surface mesh $S_{\mathrm{MRI,i}}$. For example, S_{CFD} is deformed to the target MRI surface $S_{\mathrm{MRI,6}}$, and the resulting deformed mesh is denoted as $S_{\mathrm{CFD,6}}$. This process is repeated sequentially, such that $S_{\mathrm{CFD,6}}$ is further deformed to $S_{\mathrm{MRI,7}}$, and so on, until all MRI surface meshes are matched. The cost function between the target surface mesh $S_{\mathrm{MRI,i}}$ and the resulting deformed mesh $S_{\mathrm{CFD,i}}$ is based on [23], which can be calculated as:

$$C(q,\mu) = d(\Phi_{q,\mu}\cdot S_{\mathrm{CFD,i-1}}, S_{\mathrm{MRI,i}})^2/\sigma_\epsilon^2 + R(q,\mu) \tag{1}$$

In the above equation, Φ denotes the diffeomorphism, $S_{\mathrm{CFD,i-1}}$ is the source mesh from CFD, $S_{\mathrm{MRI,i}}$ is the target mesh from MRI, d represents the varifold distance, σ_ϵ is the noise standard deviation, and R is the regularizer. The first term measures how well the targeted mesh is matched by the deformed mesh, while the second term is a regularization term that penalizes the kinetic energy of the deformations. The parameter σ_ϵ specifies the relative importance of the two terms. In the first term, d is defined as the varifold distance, which quantifies the similarity between the deformed and targeted meshes [24]. The diffeomorphism Φ is fully parameterized by the initial sets of control points q and momenta μ.

The open-source software Deformetrica 4.0 [23] was used to perform the shape registration calculation. To minimize the cost function C, the Limited-memory Broyden–Fletcher–Goldfarb–Shanno Bound (L-BFGS-B) optimizer [25], as implemented in SciPy [26], was employed. The parameters used for shape registration are listed in Table 1. The kernel width K_w specifies the spacing between control points. Here, K_w was set to 6 mm, approximately matching the diameter of the branch vessels. This value was sufficient to enable the control points to effectively capture the motion of the side branches.

For both HC and TAA, four frames of $S_{\mathrm{MRI,i}}$ were used for the shape registration (HC: $i = 3, 6, 9, 12$, TAA: $i = 3, 5, 7, 10$). To assess the effect of frame number on the flow fields, an additional calculation with eight frames of $S_{\mathrm{MRI,i}}, (i = 3-10)$ was also performed for the TAA case. After shape registration, all the surface meshes $S_{\mathrm{CFD,i}}$ contained the same number of nodes, and the time-varying geometries between $S_{\mathrm{CFD,i}}$ and $S_{\mathrm{CFD,i+1}}$ were computed using Eq. (A.3) and exported from the software. The control points and momenta of the shape registration are visualized in Fig. 3. Finally, the exact nodal coordinates of the deformed geometries at each time step were extracted and provided as input to Fluent.

Table 1
Parameters and settings used for shape registration with LDDMM in this study.

	value
K_w	6 mm
Number of control points	6120~7344
noise std σ_ϵ	1.0
convergence tolerance [27]	10^{-5}

2.3. Computational fluid dynamics equations

In this study, the Arbitrary Lagrangian–Eulerian (ALE) method is applied to solve the conservation of mass and momentum equations for the moving wall simulation. The governing transport equations for mass and momentum are presented in Eqs. (2) and (3):

$$\frac{\partial}{\partial t}\int_V \rho dV + \int_S \rho\left(\vec{v}-\vec{v}_b\right)\cdot\vec{n}\, dS = 0 \tag{2}$$

where $\vec{v}$ is the velocity vector, $\vec{v}_b$ the velocity on the boundary, $\vec{n}$ the normal vector, ρ the blood density, V the control volume, and S the surface of control volume.

$$\int_V \frac{\partial}{\partial t}(\rho\vec{v})dV + \int_S \rho\vec{v}\left(\vec{v}-\vec{v}_b\right)\cdot\vec{n}\, dS = -\int_S p\bar{\bar{I}}\cdot\vec{n}\, dS + \int_S \bar{\bar{\tau}}\cdot\vec{n}\, dS \tag{3}$$

where p is the pressure, $\bar{\bar{I}}$ is the unit tensor, and $\bar{\bar{\tau}}$ is the viscous stress tensor, $\bar{\bar{\tau}} = \mu\left(\nabla\vec{v} + \nabla\vec{v}^{\mathrm{T}}\right)$, with μ denoting dynamic viscosity.

The space conservation law can be expressed as:

$$\frac{dV}{dt} = \int_{\partial V}\vec{v}_b\cdot\vec{A} = \sum_j^{n_f}\vec{v}_{b,j}\cdot\vec{A}_j \tag{4}$$

where dV/dt is the time derivative of the arbitrary control volume V, ∂V denotes the boundary of control volume V, $\vec{A}$ is the face vector area, and n_f is the number of faces j. The dot product on the right-hand side is calculated as:

$$\vec{v}_{b,j}\cdot\vec{A}_j = \frac{\delta V_j}{\delta t} \tag{5}$$

where δV_j is the volume swept by face j of the control volume during each time step.

For the dynamic mesh, only the smoothing operation was permitted, with remeshing disabled to maintain consistent nodal connectivity throughout the simulation. A spring-based smoothing method was applied [28,29], with a maximum of 250 iterations allowed per time step to ensure optimal element quality.

The Carreau–Yasuda model [30] was used to characterize the non-Newtonian behavior of blood. This choice is justified by the shear rate distribution observed during the cardiac cycle. In both the HC and TAA cases, shear rates are typically on the order of 10^0 to 10^3 1/s. During peak systole, localized shear rates near the branch vessels can reach 10^4 1/s. Furthermore, a laminar flow assumption was adopted as reported mean Reynolds numbers [12] for these specific geometries ($\mathrm{Re_{HC}} = 1890$ and $\mathrm{Re_{TAA}} = 1480$) remain below the critical threshold for the aorta [31].

The computational settings were consistent with our previous study [12]. A pressure-based solver was used with the PISO algorithm for pressure–velocity coupling. Spatial discretization was performed using a second-order upwind scheme for convective terms and a second-order central differencing scheme for diffusive terms. Time integration was achieved via a second-order fully implicit scheme, with a constant time step of 10^{-3} s. The convergence criterion for all residuals was set to 10^{-5}.

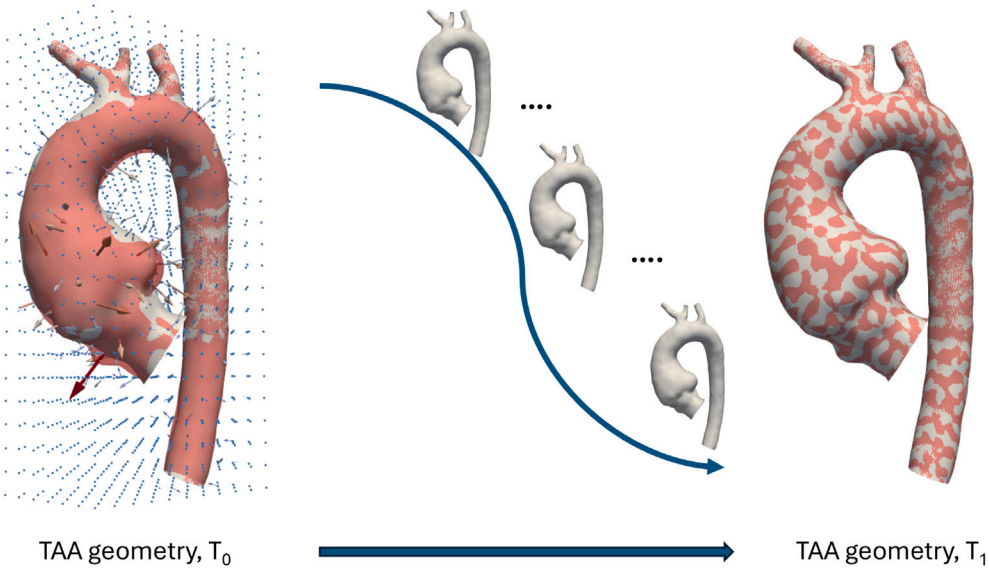

Fig. 3. Shape registration visualization: The TAA geometry at time T_0 is deformed into the geometry at time T_1. Control points are placed in the ambient space, and the corresponding momenta vectors are shown as scaled arrows. Intermediate geometries at each time step during the deformation from T_0 to T_1 are also displayed.

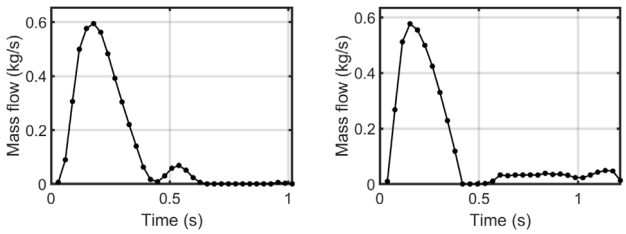

(a) HC (b) TAA

Fig. 4. Mass flow rate over one cardiac cycle obtained from 4D flow MRI for the healthy (HC) and thoracic aortic aneurysm (TAA) cases at the inlet plane.

Table 2
Ratio of outlet flow rates extracted from 4D-Flow MRI.

	ratio HC	ratio TAA
ABAO	0.66	0.55
BT	0.18	0.20
LCC	0.05	0.15
LSA	0.11	0.10

2.4. Boundary conditions

In this study, a plug flow inlet was applied, and the mass flow rates over a single cardiac cycle for both HC and TAA are shown in Fig. 4. For the CFD simulations, at least three cardiac cycles were run to ensure stable solutions.

In CFD simulation, the aorta features four flow outlets: the three primary side-branch arteries and the abdominal aorta (ABAO). The main branches consist of the branchiocephalic trunk (BT), left common carotid artery (LCC), and left subclavian artery (LSA). All four outlets were defined as the outflow boundaries, with outflow flow ratios extracted from 4D flow MRI and summarized in Table 2. For HC and TAA cases, both static and moving-wall simulations based on four-frame shape registration were conducted, referred to as HC-static, HC-4frames, TAA-static, and TAA-4frames. Additionally, a moving-wall simulation based on eight-frame shape registration was performed, named as TAA-8frames, resulting in a total of five distinct CFD simulations in this study. For the moving-wall simulations, remeshing of the volume mesh was disabled to maintain a consistent cell count during the entire calculation.

2.5. Post-processing

All CFD simulations were conducted over three consecutive cardiac cycles to ensure periodic stability of the flow fields. Hemodynamic data, specifically velocity, WSS, TAWSS and OSI, were extracted from the third cycle for post-processing and analysis. For the surface mesh at each time point, identical nodal numbering and connectivity were maintained, enabling a direct node-wise calculation of TAWSS and OSI as defined in Eqs. (6) and (7):

$$\mathrm{TAWSS} = \frac{1}{N}\sum_{i=1}^{N} \left\| \boldsymbol{\tau}_w(t_i) \right\| \tag{6}$$

$$\mathrm{OSI} = \frac{1}{2}\left(1 - \frac{\left\| \sum_{i=1}^{N} \boldsymbol{\tau}_w(t_i) \right\|}{\sum_{i=1}^{N} \left\| \boldsymbol{\tau}_w(t_i) \right\|}\right) \tag{7}$$

where N denotes the number of time steps (with a step size of 1 ms) over one cardiac cycle, t_i represents the ith time point, and $\boldsymbol{\tau}_w$ the wall shear stress vector.

To quantify the relative discrepancies between the static and dynamic simulations, the Normalized Mean Absolute Error (NMAE) was calculated following the methodology of [12], as defined in Eq. (8):

$$\mathrm{NMAE} = \frac{1}{N}\sum_{i=1}^{N} \frac{\left| \phi_{sta} - \phi_{dyn} \right|}{\frac{1}{2}\left(\phi_{sta} + \phi_{dyn} \right)} \tag{8}$$

where N is the total number of surface mesh nodes, and ϕ represents the hemodynamic metric (TAWSS or OSI) for the static and dynamic simulations at node i. The NMAE is computed in a node-wise manner, where the absolute differences at each node is normalized by the mean magnitude of the static and dynamic values and subsequently averaged over the entire surface.

Other post-processing tasks, including flow field visualization, cross-section extraction, as well as calculation of integral area and circumference, were carried out using the open-source software Paraview [32].

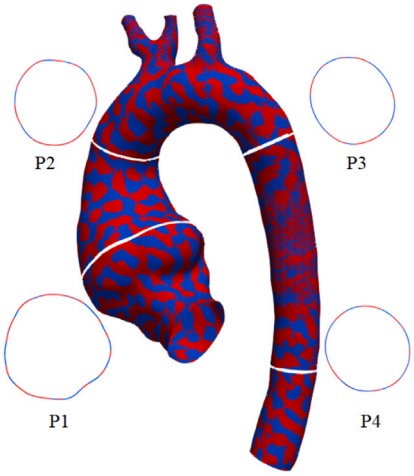

Fig. 5. Comparison between the MRI geometry and LDDMM-deformed geometry at mid-deceleration, including profiles at four representative cross-sections. The red surface represents the MRI geometry, and the blue surface shows the geometry obtained from LDDMM deformation.

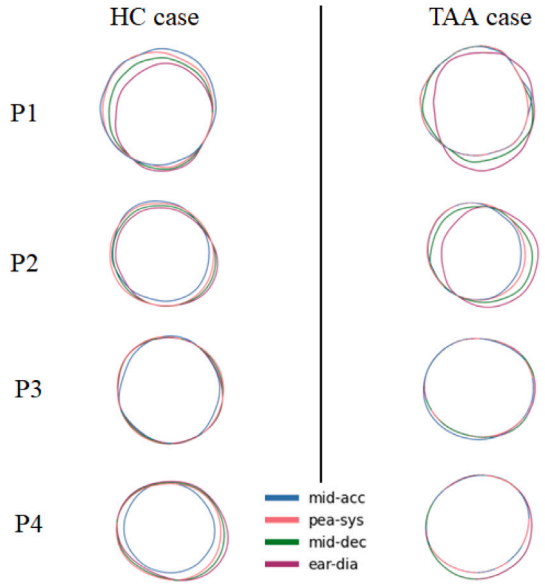

Fig. 6. Evolution of cross-sections at four key time points: mid-acceleration, peak systole, mid-deceleration, and early diastole.

3. Results

3.1. Morphing performance

Morphing performance refers to the similarity between the deformed geometry and the MRI geometry. The cost function in Eq. (1) quantifies this morphing performance. However, it is not intuitive and cannot be directly visualized. To provide visual insight into morphing performance, we compare the geometries extracted from MRI (red surface) and those obtained by LDDMM (blue surface) at the mid-deceleration phase, as shown in Fig. 5. Circumferential wall profiles are compared at four representative cross-sections: P1- proximal ascending aorta, P2- distal ascending aorta, P3- proximal descending aorta, and P4- distal descending aorta. The morphing performance is illustrated only for the TAA case, as it exhibits more complex geometrical features than the HC case. Besides the cost function, three more intuitive parameters were used to evaluate the similarity between the MRI mesh and LDDMM-morphed meshes: (1) the Hausdorff distance 'H'; (2) the integrated area 'A'; (3) the circumference 'C' of cross-sections alongside the centerlines. The comparison results and the errors between the MRI and morphing meshes are summarized in Table 3.

Table 3
Comparison of Hausdorff distance, area, and circumference between MRI and LDDMM results for the TAA case at for characteristic cardiac time instants: mid-acceleration, peak systole, mid-deceleration, and early diastole. E_A and E_C denote area and circumference errors, respectively.

	mid-acc	pea-sys	mid-dec	ear-dia
H (mm)	0.96	0.98	0.99	1.02
A_{MRI} (mm^2)	31 400.9	31 260.4	31 914.7	32 168.3
A_{LDDMM} (mm^2)	31 386.7	31 240	31 898.2	32 152.5
E_A(%)	0.045	0.065	0.052	0.049
E_C(%)	0.12	0.041	0.10	0.070

3.2. Visualization of aorta movement

The evolution of cross-sections at four key locations – proximal ascending aorta (P1), distal ascending aorta (P2), proximal descending aorta (P3) and distal descending aorta (P4) – is shown in Fig. 6. For both the HC and TAA cases, the cumulative displacement Z_{cum} was computed for each surface node over one cardiac cycle, as:

$$Z_{\text{cum}} = \sum_{i=1}^{T} \|\vec{r}_i - \vec{r}_{i-1}\| \tag{9}$$

is shown in Fig. 7. Here, $\vec{r}_i$ denotes the position of a surface node at the time i, and T represents the cardiac cycle duration in milliseconds.

3.3. Time-dependent metrics

To visualize the velocity distribution at three representative cross-sections (the proximal ascending aorta, distal ascending aorta, and proximal descending aorta) were extracted from both static and moving-wall CFD simulation results. Comparisons were performed at four distinct time instants within the cardiac cycle: mid-acceleration, peak systole, mid-deceleration, and early diastole. The resulting velocity contour matrices for the HC and TAA cases are shown in Figs. 8 and 9, respectively.

To provide a comprehensive analysis of flow fields throughout the thoracic aorta, cross-section-averaged velocity and circumferentially-averaged wall shear stress (WSS) were calculated along the centerlines for both the HC and TAA cases. These results are shown in Figs. 10 and 11, respectively. Averaged velocity and WSS distributions are plotted at four key time instants: mid-acceleration, peak systole, mid-deceleration, and early diastole.

3.4. Cycle-dependent metrics

Time-averaged wall shear stress (TAWSS) and oscillatory shear index (OSI) are important cycle-dependent metrics derived from blood flow over one cardiac cycle, widely reported in the literature for assessing the progression of aortic aneurysms. TAWSS and OSI distributions are shown on the aortic surface at peak systole for HC (Fig. 12) and TAA (Figs. 13, 14). Additionally, differences in ΔTAWSS and ΔOSI were calculated and presented. For the HC case, only differences between HC-static and HC-4frames were calculated, while for the TAA case, comparisons were made among TAA-static, TAA-4frames, and TAA-8frames. To further quantify the relative difference between static and dynamic simulations, the normalized mean absolute error (NMAE) was calculated based on the definition of [12] for all surface mesh vertices. For the HC case, TAWSS values were NMAE(4frame-static) = 18.08 ± 19.32% and the OSI yielded NMAE(4frames-static) = 46.41 ± 40.86%. For the TAA case, TAWSS values were NMAE(4frame-static) = 14.35 ± 14.16% and NMAE(8frame-static) = 15.34 ± 15.77%, while OSI results were NMAE(4frame-static) = 47.47±40.52% and NMAE(8frame-static) = 45.41 ± 40.61%.

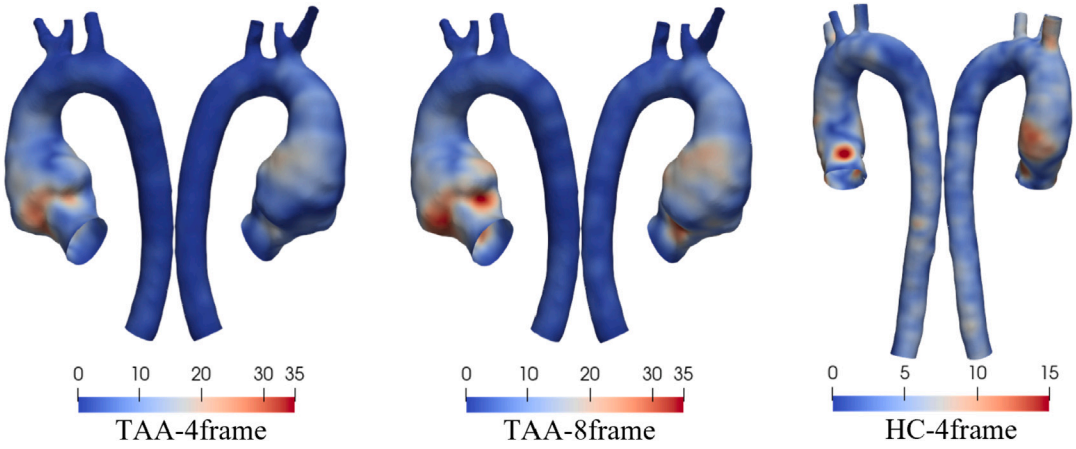

Fig. 7. Cumulative displacement (in mm) over one cardiac cycle for the thoracic aortic aneurysm (TAA) and the healthy (HC) cases.

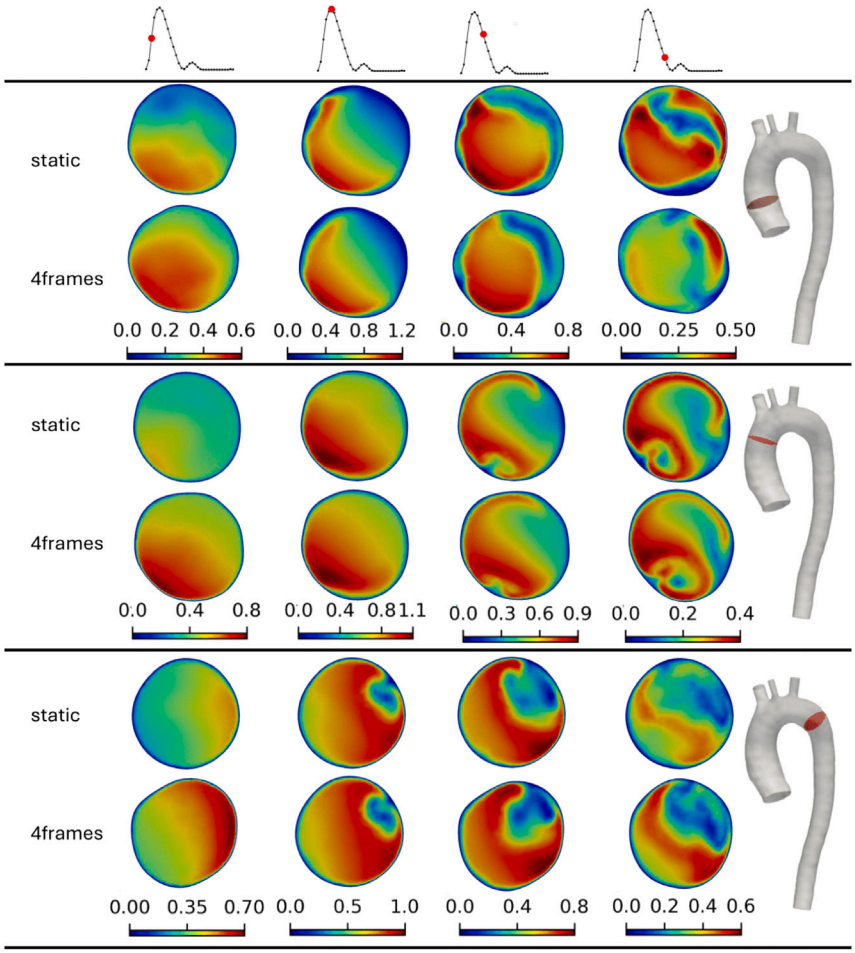

Fig. 8. Velocity magnitude (in m/s) contours at selected cross-sections for the healthy (HC) case at four key time instants. The three representative planes are located at normalized positions $L/L_0 = 0.1$, 0.2 and 0.4.

3.5. Computational time

To compare computational times between static-wall simulation and moving-wall simulations, the TAA-static, TAA-4frames, and TAA-8frames cases were run on the same node (n11-66, HPC11, ChemE, TNW, TU Delft) using 16 CPUs (Intel(R) Xeon(R) E5-2650 v4) for three full cardiac cycles. The reported computational times were 18:08:14 for TAA-static, 21:19:55 for TAA-4frames, and 21:10:06 for TAA-8frames. The increase of approximately 20% in computational time for moving-wall simulations is attributed mainly to additional operations for loading surface node coordinates and updating the volume mesh. The minor difference in simulation time between TAA-4frames and TAA-8frames (about 9 min) indicates that the complexity of wall movement does not significantly affect computational cost. Compared to [12], all simulations in this study completed more quickly, primarily due to the use of premium CPUs. Mesh deformation calculation for moving-wall simulations, performed on GPU, required approximately 8 min for the

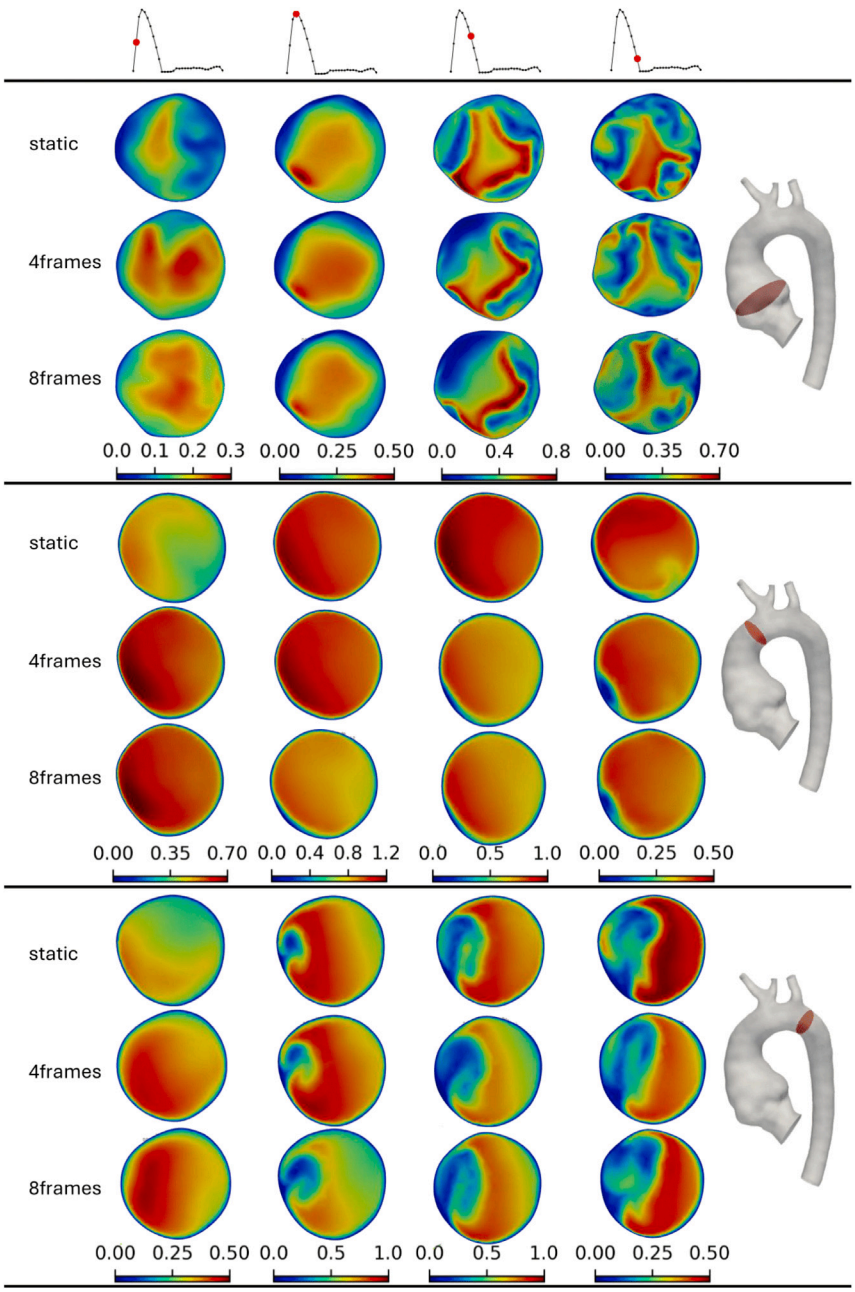

Fig. 9. Velocity magnitude (in m/s) contours at selected cross-sections for the thoracic aortic aneurysm (TAA) case at four key time instants. The three representative planes are located at normalized positions $L/L_0 = 0.1$, 0.2 and 0.4.

4-frame case and 16 min for the 8-frame case. The time required for other workflow steps, including geometry segmentation, inlet flow rate extraction, and pre-/post-processing, was negligible.

4. Discussion

4.1. Performance of shape registration

In the LDDMM-based shape registration, the kernel width was set to 6 mm, resulting in 6100-7344 control points distributed within the ambient space of the aortic geometries. The large number of control points and a clearly defined objective function ensured close agreement between the morphed results and the MRI geometries. Registration errors were found to be comparable to the errors introduced by grid remeshing, highlighting the robustness of the morphing method. A high density of control points enabled accurate capture of movement throughout the thoracic aorta, including all branches. For reliable surface morphing near branches, it is recommended that each branch length be at least twice the kernel width to guarantee adequate control point coverage in branch zones and to minimize interference from the main aortic surface. If branches obtained from MRI are too short, flow extensions can be added, as was done in the HC case.

Owing to the diffeomorphic nature of registration, the structural integrity of the surface is preserved, preventing any non-physiological deformation. In addition to generating the morphed geometry, Deformetrica also produces the full trajectory of movement from the initial to the target mesh, thereby eliminating the need for separate interpolation steps as required in previous studies.

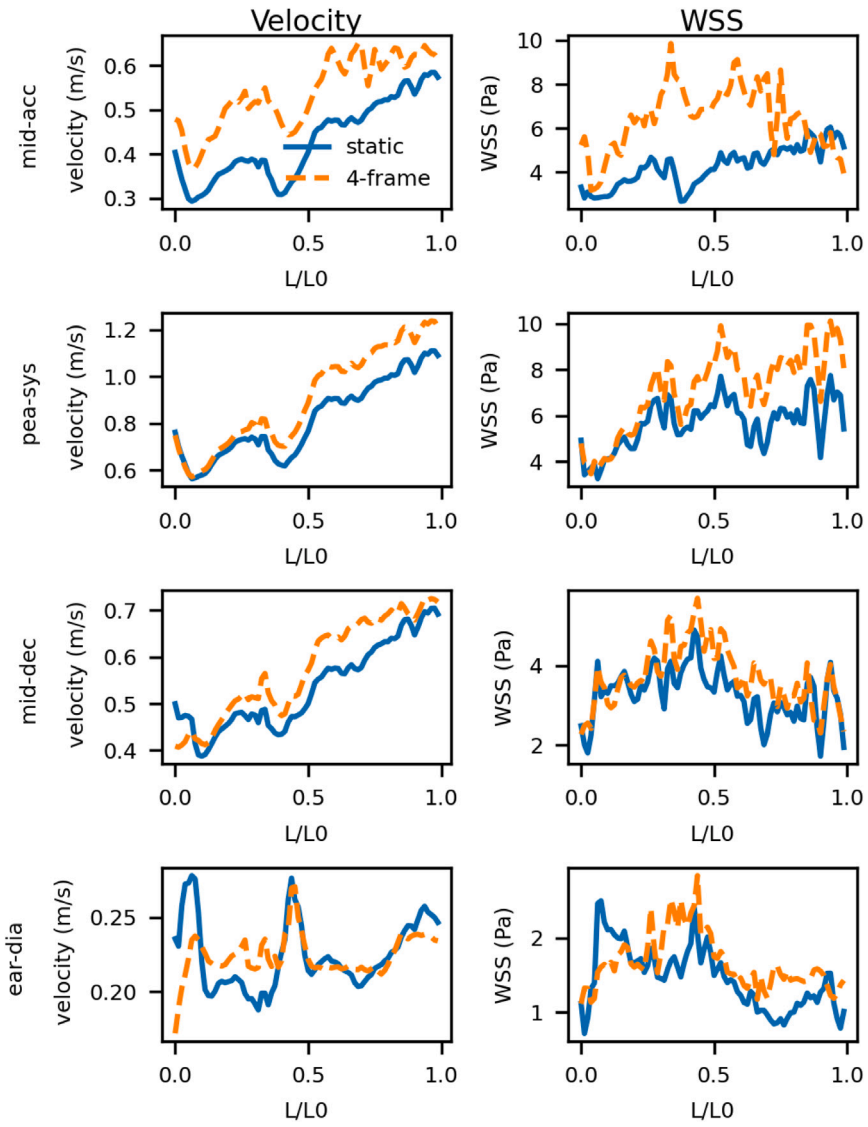

Fig. 10. Cross-section averaged velocity and wall shear stress (WSS) along the aortic centerline for the healthy (HC) case. Each row corresponds to a distinct time instant: mid acceleration, peak systole, mid-deceleration, and early diastole. The two columns show velocity and wall shear stress (WSS), respectively. For each time instant, results from both static and moving-wall simulations are presented for comparison.

4.2. Effect of wall movement on time-dependent metrics

The analysis of time-dependent metrics focuses on four key time instants within the cardiac cycle. At mid-acceleration and early diastole, whether for the HC or TAA case, velocity and wall shear stress in moving-wall simulations exhibited significant deviations from the static-wall simulations across the aorta. Notably, for the TAA case, the 4-frame and 8-frame moving-wall simulations showed good agreement. At peak systole and mid-deceleration, velocity and wall shear stress were generally consistent between static and moving-wall simulations in the ascending aorta region ($L/L_0 < 0.5$). For the HC case, larger deviations appeared between static and moving-wall simulations in the descending aorta ($L/L_0 > 0.5$). In the TAA case, moving-wall simulations also presented differences in the descending aorta compared to static-wall results. Nevertheless, both simulation approaches exhibited similar overall trends.

However, at the proximal ascending aorta cross-section for the TAA case (Fig. 9), the velocity distribution differs noticeably between static-wall and moving-wall simulations. Overall, when considering centerline-averaged flow fields for both the HC and TAA cases, moving-wall simulations align well with static-wall simulations during peak systole and mid-deceleration. In contrast, at early diastole and mid-acceleration, larger deviations are observed between the two approaches. When examining detailed flow field patterns, the static and moving-wall simulations reveal distinct differences, particularly within aneurysmal regions.

4.3. Effect of wall movement on cycle-dependent metrics

Given that this study effectively captures the movement of the thoracic aorta, significant differences in cycle-dependent metrics are observed between static and wall-moving simulations. As shown in Fig. 13, within the aneurysm and branch regions, moving-wall simulations (TAA-4frames and TAA-8frames) exhibit higher time-averaged wall shear stress (TAWSS) compared to the static simulation. This increase arises from the more complex motion at the aneurysm surface, which in turn generates more intricate flow patterns. However, the difference in TAWSS between the TAA-8frames and TAA-4frames simulations is confined to the aneurysm surface and does not extend to the branches.

For the OSI shown in Fig. 14, significant differences between static and moving-wall simulations are also evident on the aneurysm surface. At the branches, however, OSI shows little variation between the

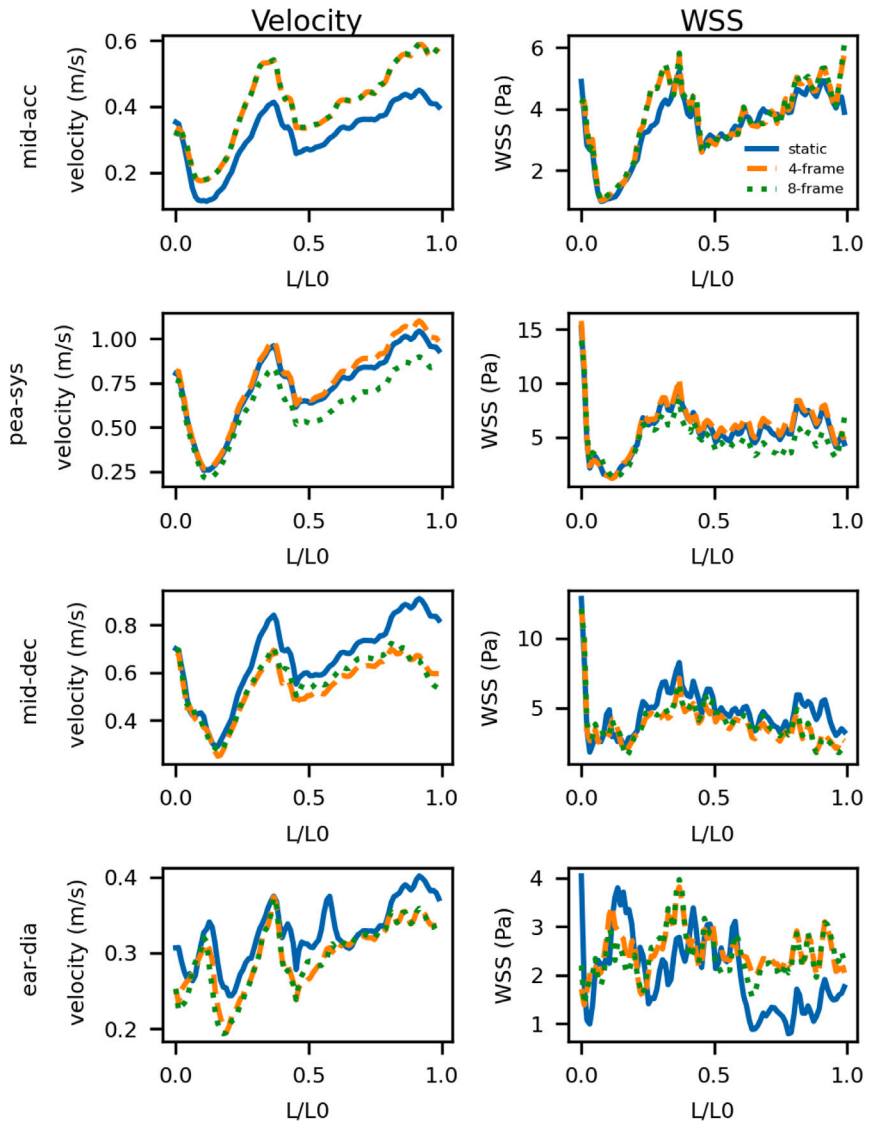

Fig. 11. Cross-section averaged velocity and wall shear stress (WSS) along the aortic centerline for the thoracic aortic aneurysm (TAA) case. Each row corresponds to a distinct time instant: mid-acceleration, peak systole, mid-deceleration, and early diastole. The two columns display velocity and wall shear stress (WSS), respectively. Results for static simulation, as well as the 4-frame and 8-frame moving-wall simulations, are shown in each subfigure for comparison.

two simulation types. In contrast, for the HC case (Fig. 12), there is no significant difference on the main aorta between static and moving-wall simulations. On the main aorta surface, the TAWSS in the moving-wall simulation is only about 1Pa higher than in the static simulation. Significant TAWSS differences are observed on the branches of the HC aorta, likely due to lower segmentation quality in these regions, causing marked diameter variations between phases. Even after adding a 15 mm flow extension to the branches, these abnormal movements persist in CFD simulations, leading to increased TAWSS near the branches. For the OSI in the HC case, no clear regional differences are apparent. Therefore, to accurately capture TAWSS or OSI values in specific regions (e.g., aneurysm surface), it is essential to incorporate aortic wall movement in CFD modeling.

4.4. Effect of frame numbers on moving-wall simulations

For time-dependent metrics such as velocity and WSS, both the velocity patterns (Fig. 9) and the centerline-averaged values (Fig. 11) show that the TAA-4frames simulation generally agrees well with the TAA-8frames results. Similarly, for cycle-dependent metrics (TAWSS and OSI), the TAA-4frames and TAA-8frames simulations exhibit comparable deviations from the static simulations, as evidenced by the mean absolute error calculations and contour differences (8frame minus 4frame) shown in Figs. 13 and 14. One reason is that increasing the number of MRI frames does not significantly alter the overall aortic movement characteristics. Another reason is that wall movement occurs during only about 30% of the cardiac cycle in these simulations, while for the remaining 70%, the aorta remains static.

4.5. Comparison with previous work based on the RBF approach

The motion prescription approach from our previous study based on the radial-basis function (RBF) method, [12] has been repeated here for comparison with the current study. Based on the author's experience, the advantages and disadvantages of both methods are summarized as follows:

User-Friendliness: In this study, motion prescription is streamlined and user-friendly, implemented via a simple Python loop code based on Deformetrica 4.0 software. The only user input required is the deformation kernel width, K_w. By contrast, the previous study required multiple software tools and manual inputs: (i) VMTK was used to

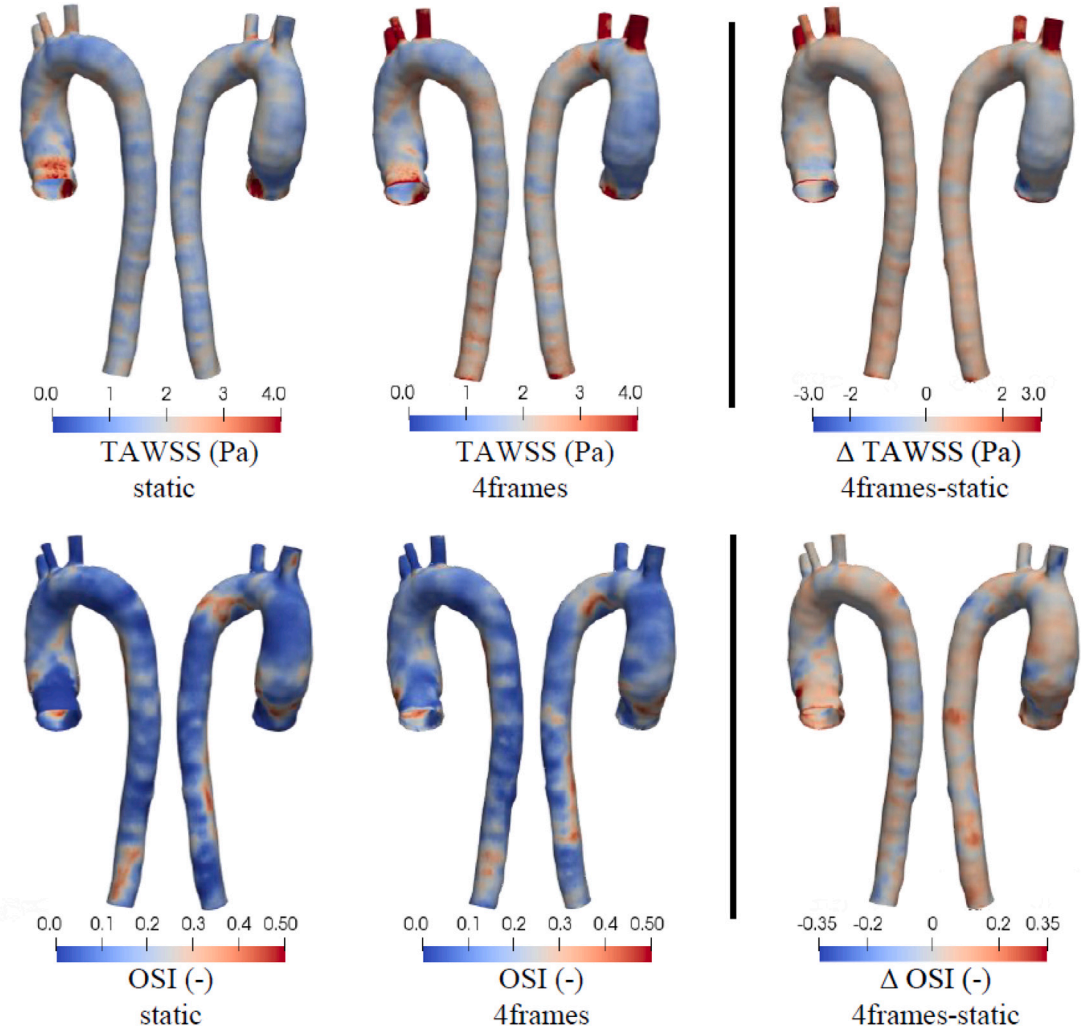

Fig. 12. Distributions of time-averaged wall shear stress (TAWSS, Pa) and oscillatory shear index (OSI) for the healthy (HC) case. Results are presented for both static and 4-frame moving-wall simulations, along with their differences.

generate aortic centerlines and diameters; (ii) MATLAB code created control-point pairs; (iii) the Python package pyGem performed RBF interpolation; (iv) manual adjustment of control points was necessary to optimize morphing performance, and (v) finally, time–space interpolation generated the full cardiac cycle motion. Due to the significantly reduced complexity and integration, the method developed in this study is considered more user-friendly.

Morphing performance: In our previous study, the nodes on the aortic mesh were assumed to move primarily along the radial direction, and control point pairs were selected based on anatomical features. In contrast, this study aims to optimize the similarity between the morphed mesh and the target mesh, allowing for more degrees of freedom in capturing the complex movements of the aortic surface. Consequently, this study employs approximately 60 times more control points than the prior one, enabling the LDDMM approach to achieve superior morphing performance. The current method effectively captures the movement of the thoracic aorta, including the branches. Previously, branch movement had to be neglected due to the difficulty of placing sufficient control points on the branches.

Time-consumption: Strictly speaking, LDDMM calculations are more computationally expensive than RBF interpolation. For LDDMM, a GPU computation typically requires approximately 16 min, whereas RBF interpolation can be completed within seconds on a CPU. However, the LDDMM GPU calculation is practical on modern workstations, as it only requires about 100 MB of GPU memory.

It should be noted that this study does not aim to directly compare deformation models like LDDMM and RBF. The characteristics and performance of these models have been extensively reviewed in the literature [19,33,34]. Instead, our goal is to introduce tools from medical image analysis into the field of compliant CFD modeling. Here, we demonstrated how the medical image registration tools such as Deformetrica can be applied to provide high-quality mesh morphing performance while simplifying complex workflows.

5. Limitations of present study

Limitation of MRI dataset: The present analysis is limited by the availability of a small 4D Flow MRI dataset for the TAA and HC cases, and therefore serves primarily as a proof-of-concept study. Although eight MRI frames were used, extracting aortic geometries beyond early diastole remains challenging. Furthermore, this study did not investigate the uncertainty arising from MRI segmentation nor its impact on CFD results.

Limitation of shape registration: To reconstruct the aortic motion trajectory throughout the full cardiac cycle, we applied a piecewise shape registration approach, where independent registrations were performed between successive time points (e.g., from t_0 to t_1, then from t_1 to t_2). This piecewise framework ensures geometric continuity (C^0) and a smooth, diffeomorphic transformation within each open interval. However, it does not inherently guarantee higher-order smoothness (C^1

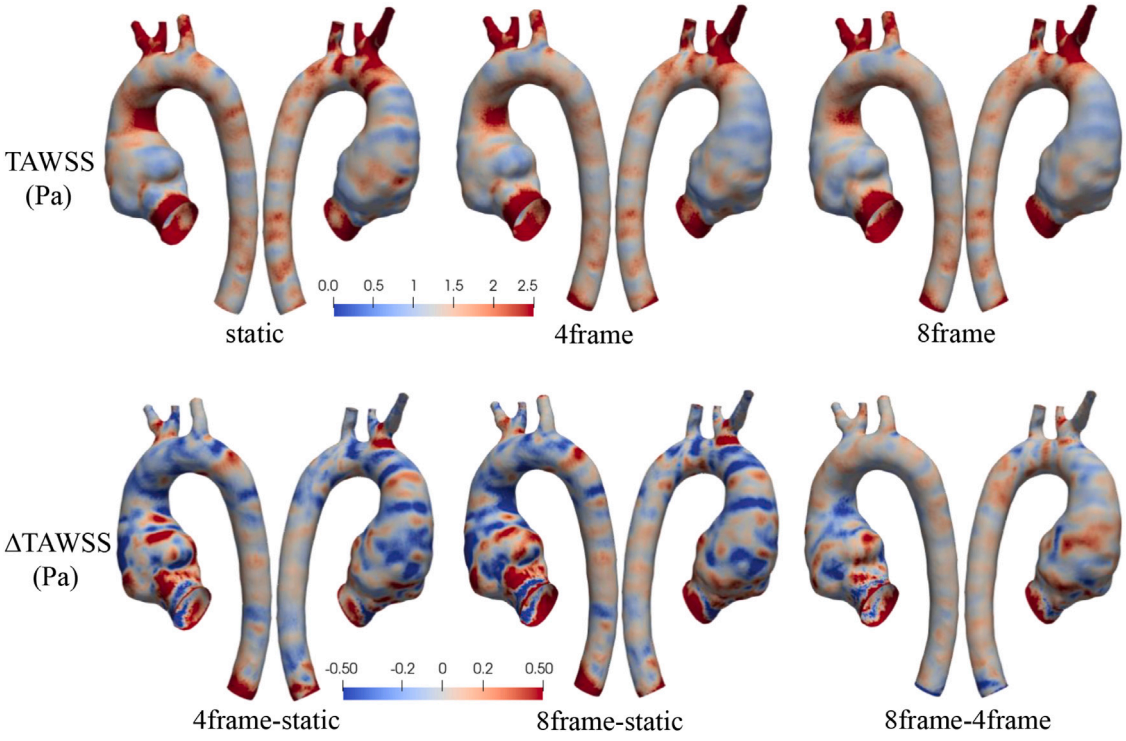

Fig. 13. TAWSS (Pa) and differences (ΔTAWSS (Pa)) for the TAA case: static, 4-frame dynamic, and 8-frame dynamics simulations are compared. ***4frame-static***: Difference between 4-frame dynamic and static simulations; ***8frame-static***: Difference between 8-frame dynamic and static simulations; ***8frame-4frame***: Difference between 8-frame and 4-frame dynamic simulations;.

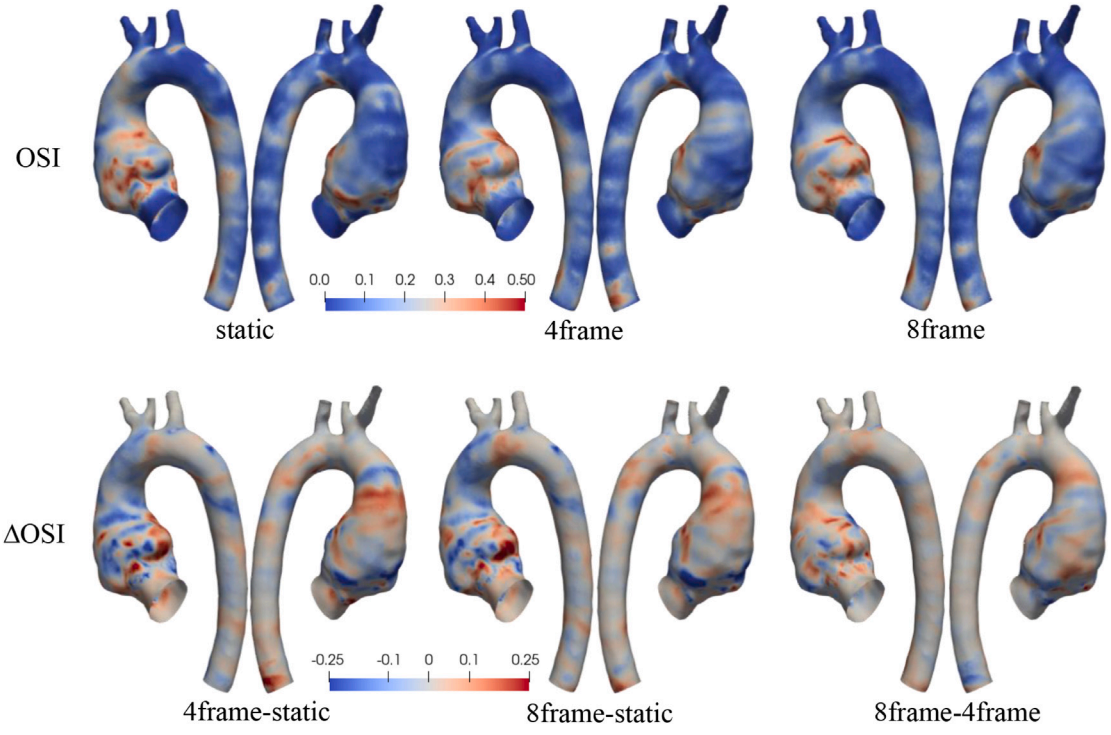

Fig. 14. OSI and differences (ΔOSI) for the TAA case: static, 4-frame dynamic, and 8-frame dynamic simulations are compared. ***4frame-static***: Difference between 4-frame dynamic and static simulations; ***8frame-static***: Difference between 8-frame dynamic and static simulations; ***8frame-4frame***: Difference between 8-frame and 4-frame dynamic simulations;.

continuity) at the discrete interval endpoints, such as t_0 or t_1. In this study, geodesic regression with LDDMM was applied to model aortic movement trajectories using 4 or 8 MRI frames. Although geodesic regression can ensure the overall smoothness of the trajectory, it is computationally expensive (approximately 10 h) and yields only linear regression, which compromises morphing performance. Therefore,

considering both calculation cost and morphing quality, the standard shape registration approach was selected for this study.

Limitation of loss function: A significant limitation of the LDDMM framework, specifically regarding the loss function in Eq. (1), is that it does not explicitly account for mesh quality during the optimization process. The current formulation lacks penalty terms to mitigate poor element shapes, such as excessive skewness or element stretching (i.e., a 'mesh-aware' penalty). As suggested by [35], incorporating a mesh-quality regularization term into the loss function would generate deformed meshes better suited for high-fidelity CFD simulations.

6. Conclusions and outlook

Following our previous work in image-based compliant aorta modeling based on the Radial Basis Function (RBF) interpolation [12], the present study introduces a novel simulation framework based on LDDMM. This framework significantly simplifies the pre-processing workflow for CFD simulations and is more user-friendly. It also improves morphing performance and provides more physiologically realistic aortic motion for CFD analyses. The errors resulting from grid deformation are comparable to those from grid remeshing, supporting the robustness and reliability of the mesh-morphing approach. By incorporating thousands of control points, this method enables the movement of the thoracic aorta, including side-branches, to be captured within CFD simulations.

For both aortic geometries considered, substantial differences in hemodynamic biomarkers were observed between static and moving-aorta simulations. In the healthy case, differences of 18% in time-averaged wall shear stress (TAWSS) and 46% in oscillatory shear index (OSI) were obtained. Similarly, for the thoracic aortic aneurysm case, these values were 14% and 47%, respectively. These results underscore the importance of accounting for aortic wall motion in CFD simulations to obtain accurate hemodynamic biomarkers.

However, MRI-based compliant simulation are highly dependent on the quality of MRI segmentation. Currently, only a limited number of MRI frames (4-8) were used for simulation. Moreover, the uncertainty arising from MRI image segmentation has not yet been addressed. In future work, we plan to apply AI-based segmentation tools to extract additional frames for compliant aorta modeling and to quantify the uncertainty introduced by MRI segmentation.

List of abbreviations:

ABAO	Abdominal Aorta
ALE	Arbitrary Lagrangian-Eulerian
ASC	Ascending Aorta
BT	Brachiocephalic Trunk
CFD	Computational Fluid Dynamics
DESC	Descending Aorta
FSI	Fluid Structure Interaction
HC	Healthy Control
LCC	Left Common Carotid Artery
LDDMM	Large Deformation Diffeomorphic Metric Mapping
LSA	Left Subclavian Artery
MBM	Moving Boundary Method
MRI	Magnetic Resonance Imaging
OSI	Oscillatory Shear Index
RBF	Radial Basis Function
TAA	Thoracic Aortic Aneurysm
TAWSS	Time-Averaged Wall Shear Stress
VMTK	Vascular Modeling Toolkit
WSS	Wall Shear Stress

CRediT authorship contribution statement

Daiqi Lin: Writing – review & editing, Writing – original draft, Validation, Software, Methodology, Investigation. **Jos Westenberg:** Writing – review & editing, Data curation. **Hildo Lamb:** Writing – review & editing, Data curation. **Saša Kenjereš:** Writing – review & editing, Writing – original draft, Supervision, Resources, Methodology, Conceptualization.

Ethics approval and consent to participate

This study protocol was approved by the Medical Ethics Committee (METC) of the Leiden University Medical Center (number P18.034 for healthy volunteer and G20.149 for patient) and both subjects signed a consent to participate.

Declaration of competing interest

The authors declare that they have no known competing financial interests or personal relationships that could have appeared to influence the work reported in this paper.

Acknowledgments

The research of Daiqi Lin was made possible by the financial support of the Chinese Scholarship Council (CSC). The authors acknowledge the use of computational resources of the DelftBlue supercomputer and HPC11, provided by Delft High Performance Computing Centre.[1] This research was also partially supported by a grant from the Dutch Heart Foundation, The Netherlands (Grant Number CVON2018-08-RADAR) .

Appendix A. Theoretical background of LDDMM

Detailed introductions to the theoretical background of LDDMM behind the software Deformetrica are provided by Bône et al. [23] and Durrleman et al. [36]. Here, we give a concise summary of the theory, covering diffeomorphism, shape distance, and cost function, to help readers understand its application in 3D shape registration. To generate deformations of 3D shapes, a set of n control points $(q_i)_{i=1,\dots,n}$ is introduced into the ambient space of the shape, with corresponding 'momentum' vectors $(\mu_i)_{i=1,\dots,n}$ attached to these control points. Those paired define a 'velocity' vector field v of the ambient space through a convolution filter:

$$v(x) = \sum_{i=1}^{n} K(x, q_i) \cdot \mu_i \tag{A.1}$$

where K is typically a Gaussian kernel:

$$K(x, y) = \exp\left(-\frac{\|x - y\|^2}{\sigma^2}\right) \tag{A.2}$$

with kernel width $\sigma > 0$.

To obtain a time-varying velocity field $v(x,t)$ that can be computed at any time t using Eq. (A.1), evolution equations are prescribed for the control point and momentum sets based on the Hamiltonian equations:

$$\begin{cases} \dot{q}(t) = K[q(t), q(t)] \cdot \mu(t) \\ \dot{\mu}(t) = -\frac{1}{2}\nabla_q \left\{ K[q(t), q(t)] \cdot \mu(t)^T \mu(t) \right\} \end{cases} \tag{A.3}$$

From Eqs. (A.1),(A.3), the mapping $\Phi_{q,\mu}$ can be obtained, which is a diffeomorphism of the ambient space fully parameterized by the

[1] www.tudelft.nl/dhpc

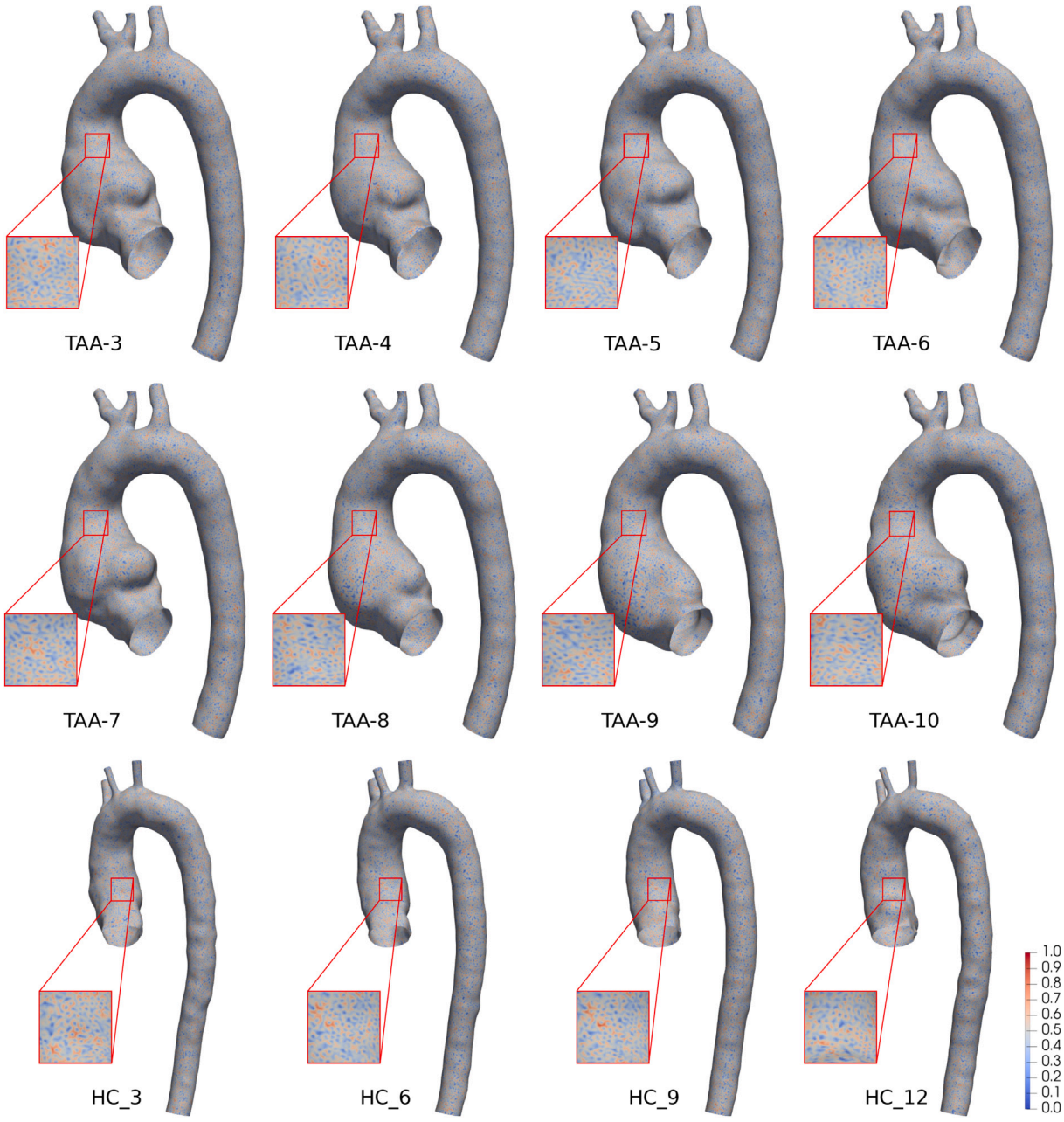

Fig. B.15. Spatial distribution of the morphing error (mm), defined as the minimum distance from each deformed surface node to the corresponding MRI-derived geometry. The shared colorbar (0-1 mm) is provided in the final subfigure.

initial sets of control points q and momentum μ. In shape registration, the objective is to optimize the initial value of the control points and momenta to estimate the desired transformation. In deforming shapes, another important concept is the distance between two shapes, or shape attachment, which indicates how close the two shapes are. For meshes with point-to-point correspondence, the Euclidean l^2 distance can be used. However, for more general meshes without such correspondence, either the current distance [37]

$$d\left((n_k^\alpha, c_k^\alpha)_{k=1,\dots,r^\alpha}, (n_l^\beta, c_l^\beta)_{l=1,\dots,r^\beta}\right)^2 = \sum_k \sum_l K_W(c_k^\alpha, c_l^\beta) \cdot (n_k^\alpha)^\top n_l^\beta \tag{A.4}$$

or the varifold distance [24] can be calculated.

$$d\left((n_k^\alpha, c_k^\alpha)_{k=1,\dots,r^\alpha}, (n_l^\beta, c_l^\beta)_{l=1,\dots,r^\beta}\right)^2 = \sum_k \sum_l K_W(c_k^\alpha, c_l^\beta) \cdot \frac{\left((n_k^\alpha)^\top n_l^\beta\right)^2}{\|n_k^\alpha\| \, \|n_l^\beta\|} \tag{A.5}$$

Here $(c_k)_{k=1,\dots,r}$ are the edge centers of the mesh, $(n_k)_{k=1,\dots,r}$ are the edge normals, and K_W is a Gaussian kernel with width σ_W.

Once the diffeomorphic transformation $\Phi_{q,\mu}$ and the shape distances d have been defined, the shape registration between two shapes S_1, S_2 can be formulated as an optimization problem on the loss function [23]:

Table C.4
Volumetric mesh quality metrics for the HC and TAA cases across representative temporal phases. Note: The symbol '↑' denotes that values closer to 1 indicate superior mesh quality (ideal orthogonality), whereas '↓' denotes that values closer to 0 indicate superior quality (minimal skewness).

Case	Time-point	Orthogonal quality ↑	Cell equiangle skew ↓	Cell equivolume skew ↓
HC	mid-acc	0.71 ± 0.06	0.36 ± 0.05	0.29 ± 0.07
	pea-sys	0.74 ± 0.04	0.33 ± 0.03	0.25 ± 0.04
	mid-dec	0.74 ± 0.05	0.34 ± 0.04	0.26 ± 0.05
	ear-dia	0.71 ± 0.08	0.36 ± 0.05	0.29 ± 0.08
TAA	mid-acc	0.73 ± 0.06	0.35 ± 0.05	0.27 ± 0.06
	pea-sys	0.75 ± 0.04	0.34 ± 0.03	0.25 ± 0.04
	mid-dec	0.73 ± 0.05	0.35 ± 0.04	0.27 ± 0.05
	ear-dia	0.69 ± 0.10	0.37 ± 0.06	0.31 ± 0.10

$$C(q,\mu) = d(\Phi_{q,\mu} \cdot S_1, S_2)^2/\sigma_\epsilon^2 + R(q,\mu) \tag{A.6}$$

where the first term quantifies the shape attachment, i.e. how well the deformation of the first shape corresponds to the second shape. The second term acts as a regularizer, requiring the deformation to have low energy. The trade-off between attachment and regularization is controlled by the noise standard deviation σ_ϵ.

Appendix B. Morphing accuracy of deformed meshes

To visualize the registration accuracy of the LDDMM framework, the minimum Euclidean distances between the nodes of the deformed meshes and their corresponding MRI-derived surfaces were computed, Fig. B.15. A total of 12 temporal phases from both the HC and TAA cases were included in this analysis. All subfigures show errors within a consistent range of 0–1 mm and utilize a shared color scale for direct comparison. As illustrated, the majority of the surface nodes exhibit an error of approximately 0.5 mm, represented by the light gray regions in the figure.

Appendix C. Mesh quality

The volumetric mesh quality metrics were exported from Ansys Fluent for both the static and dynamic cases. While the mesh at peak systole was originally generated using ICEM-CFD (Ansys, Canonsburg, PA, USA), the meshes for all other temporal points were generated by deforming the peak-systolic template using the spring-based smoothing method in Ansys Fluent, [28,29]. To ensure numerical stability, the orthogonal quality and skewness were monitored throughout the deformation process. As summarized in Table C.4, these metrics remained within highly acceptable limits for all analyzed time points.

References

[1] J.A. Elefteriades, E.A. Farkas, Thoracic aortic aneurysm: clinically pertinent controversies and uncertainities, J. Am. Coll. Cardiol. 55 (2010) 841–857.
[2] J.Z. Goldfinger, J.L. Halperin, M.L. Marin, A.S. Stewart, K.A. Eagle, V. Fuster, Thoracic aortic aneurysm and dissection, J. Am. Coll. Cardiol. 64 (2014) 1725–1739.
[3] E.M. Senser, S. Misra, S. Henkin, Thoracic aortic aneurysm: a clinical review, Cardiol. Clin. 39 (2021) 505–515.
[4] M. Ramaekers, B.P. Adriaans, J.F. Juffermans, H.C. Van Assen, S. Bekkers, A. Scholte, S. Kenjeres, H. Lamb, J.E. Wildberger, J. Westenberg, S. Schalla, Characterization of ascending aortic flow in patients with degenerative aneurysms: a 4D flow magnetic resonance study, Invest. Radiol. 56 (2021) 494–500.
[5] S. Kenjereš, On recent progress in modelling and simulations of multi-scale transfer of mass, momentum and particles in bio-medical applications, Flow, Turbul. Combust. 96 (2016) 837–860.
[6] M. Ramaekers, I. van der Vlugt, J.J. Westenberg, R. Perinajová, H.J. Lamb, J.E. Wildberger, S. Kenjereš, S. Schalla, Flow patterns in ascending aortic aneurysms: Determining the role of hypertension using phase contrast magnetic resonance and computational fluid dynamics, Comput. Biol. Med. 172 (2024) 108310.
[7] M. Alimohammadi, J.M. Sherwood, M. Karimpour, O. Agu, S. Balabani, V. Díaz-Zuccarini, Aortic dissection simulation models for clinical support: fluid-structure interaction vs. rigid wall models, Biomed. Eng. Online 14 (2015) 1–16.
[8] P. Reymond, P. Crosetto, S. Deparis, A. Quarteroni, N. Stergiopulos, Physiological simulation of blood flow in the aorta: comparison of hemodynamic indices as predicted by 3-D FSI, 3-D rigid wall and 1-D models, Med. Eng. Phys. 35 (6) (2013) 784–791.
[9] Y. Qiao, Y. Zeng, Y. Ding, J. Fan, K. Luo, T. Zhu, Numerical simulation of two-phase non-Newtonian blood flow with fluid-structure interaction in aortic dissection, Comput. Methods Biomech. Biomed. Eng. 22 (6) (2019) 620–630.
[10] R. Pons, A. Guala, J.F. Rodríguez-Palomares, J. Cajas, L. Dux-Santoy, G. Teixidó-Tura, J.J. Molins, M. Vázquez, A. Evangelista, J. Martorell, Fluid–structure interaction simulations outperform computational fluid dynamics in the description of thoracic aorta haemodynamics and in the differentiation of progressive dilation in Marfan syndrome patients, R. Soc. Open Sci. 7 (2) (2020) 191752.
[11] E. Vignali, E. Gasparotti, S. Celi, S. Avril, Fully-coupled FSI computational analyses in the ascending thoracic aorta using patient-specific conditions and anisotropic material properties, Front. Physiol. 12 (2021) 732561.
[12] R. Perinajová, T. van de Ven, E. Roelse, F. Xu, J. Juffermans, J. Westenberg, H. Lamb, S. Kenjereš, A comprehensive MRI-based computational model of blood flow in compliant aorta using radial basis function interpolation, BioMedical Eng. OnLine 23 (69) (2024) 1–28.
[13] M.-K. Ganten, T.F. Weber, H. von Tengg-Kobligk, D. Böckler, W. Stiller, P. Geisbüsch, G.W. Kauffmann, S. Delorme, M. Bock, H.-U. Kauczor, Motion characterization of aortic wall and intimal flap by ECG-gated CT in patients with chronic B-dissection, Eur. J. Radiol. 72 (1) (2009) 146–153.
[14] M. Bonfanti, S. Balabani, J.P. Greenwood, S. Puppala, S. Homer-Vanniasinkam, V. Díaz-Zuccarini, Computational tools for clinical support: a multi-scale compliant model for haemodynamic simulations in an aortic dissection based on multi-modal imaging data, J. R. Soc. Interface 14 (136) (2017) 20170632.
[15] M. Bonfanti, S. Balabani, M. Alimohammadi, O. Agu, S. Homer-Vanniasinkam, V. Díaz-Zuccarini, A simplified method to account for wall motion in patient-specific blood flow simulations of aortic dissection: Comparison with fluid-structure interaction, Med. Eng. Phys. 58 (2018) 72–79.
[16] K. Capellini, E. Vignali, E. Costa, E. Gasparotti, M.E. Biancolini, L. Landini, V. Positano, S. Celi, Computational fluid dynamic study for aTAA hemodynamics: an integrated image-based and radial basis functions mesh morphing approach, J. Biomech. Eng. 140 (11) (2018) 111007.
[17] K. Capellini, E. Gasparotti, U. Cella, E. Costa, B.M. Fanni, C. Groth, S. Porziani, M.E. Biancolini, S. Celi, A novel formulation for the study of the ascending aortic fluid dynamics with in vivo data, Med. Eng. Phys. 91 (2021) 68–78.
[18] K. Calò, K. Capellini, G. De Nisco, V. Mazzi, E. Gasparotti, D. Gallo, S. Celi, U. Morbiducci, Impact of wall displacements on the large-scale flow coherence in ascending aorta, J. Biomech. 154 (2023) 111620.
[19] M. Wang, P. Li, A review of deformation models in medical image registration, J. Med. Biological Eng. 39 (2019) 1–17.
[20] D. Lin, S. Kenjereš, Towards fast and reliable estimations of 3D pressure, velocity and wall shear stress in aortic blood flow: CFD-based machine learning approach, Comput. Biol. Med. 191 (2025) 110137.
[21] P. Hilhorst, S. Verstraeten, K. Zajac, R. Ganesan, M. van't Veer, F. van de Vosse, W. Huberts, A statistical shape modeling approach for the derivation of a data-driven geometry-aware lumped arterial stenosis model, Int. J. Numer. Methods Biomed. Eng. 42 (2) (2026) e70138.
[22] L. Antiga, M. Piccinelli, L. Botti, B. Ene-Iordache, A. Remuzzi, D.A. Steinman, An image-based modeling framework for patient-specific computational hemodynamics, Med. Biol. Eng. Comput. 46 (2008) 1097–1112.
[23] A. Bône, M. Louis, B. Martin, S. Durrleman, Deformetrica 4: an open-source software for statistical shape analysis, in: Shape in Medical Imaging: International Workshop, ShapeMI 2018, Held in Conjunction with MICCAI 2018, Granada, Spain, September 20, 2018, Proceedings, Springer, 2018, pp. 3–13.
[24] N. Charon, A. Trouvé, The varifold representation of nonoriented shapes for diffeomorphic registration, SIAM J. Imaging Sci. 6 (4) (2013) 2547–2580.
[25] R.H. Byrd, P. Lu, J. Nocedal, C. Zhu, A limited memory algorithm for bound constrained optimization, SIAM J. Sci. Comput. 16 (5) (1995) 1190–1208.
[26] P. Virtanen, R. Gommers, T.E. Oliphant, M. Haberland, T. Reddy, D. Cournapeau, E. Burovski, P. Peterson, W. Weckesser, J. Bright, et al., SciPy 1.0: fundamental algorithms for scientific computing in Python, Nature Methods 17 (3) (2020) 261–272.

[27] AramisLab, ICM Institute, LDDMM – deformetrica wiki, 2019, URL https://gitlab.com/icm-institute/aramislab/deformetrica/-/wikis/1_lddmm. Last edited by Alexandre Bône on Oct 17, 2019.
[28] F.J. Blom, Considerations on the spring analogy, Internat. J. Numer. Methods Fluids 32 (6) (2000) 647–668.
[29] C. Degand, C. Farhat, A three-dimensional torsional spring analogy method for unstructured dynamic meshes, Comput. Struct. 80 (3–4) (2002) 305–316.
[30] K. Yasuda, R. Armstrong, R. Cohen, Shear flow properties of concentrated solutions of linear and star branched polystyrenes, Rheol. Acta 20 (2) (1981) 163–178.
[31] A.F. Stalder, M. Russe, A. Frydrychowicz, J. Bock, J. Hennig, M. Markl, Quantitative 2D and 3D phase contrast MRI: optimized analysis of blood flow and vessel wall parameters, Magn. Reson. Med.: An Off. J. Int. Soc. Magn. Reson. Med. 60 (5) (2008) 1218–1231.
[32] A.H. Squillacote, J. Ahrens, C. Law, B. Geveci, K. Moreland, B. King, The Paraview guide, vol. 366, Kitware Clifton Park, NY, 2007.
[33] F.P. Oliveira, J.M.R. Tavares, Medical image registration: a review, Comput. Methods Biomech. Biomed. Eng. 17 (2) (2014) 73–93.
[34] A. Sotiras, C. Davatzikos, N. Paragios, Deformable medical image registration: A survey, IEEE Trans. Med. Imaging 32 (7) (2013) 1153–1190.
[35] J. Chen, L. Qian, R. Gong, C. Sun, T. Qin, T. Pham, C. Martin, M. Zafar, J. Elefteriades, W. Sun, L. Liang, A computational pipeline for patient-specific modeling of thoracic aortic aneurysm: From medical image to finite element analysis, in: Medical Imaging 2026: Clinical and Biomedical Imaging, Edited By Barjor S. Gimi, Andrzej Krol, Proc. of SPIE Vol. 13929, 139291B, SPIE, 2026, pp. 1–8.
[36] S. Durrleman, M. Prastawa, N. Charon, J.R. Korenberg, S. Joshi, G. Gerig, A. Trouvé, Morphometry of anatomical shape complexes with dense deformations and sparse parameters, NeuroImage 101 (2014) 35–49.
[37] M. Vaillant, J. Glaunes, Surface matching via currents, in: Biennial International Conference on Information Processing in Medical Imaging, Springer, 2005, pp. 381–392.